

# Electrochemical Phase Transition: The Heartcore of Modern Energy Technologies

Keyvan Malaie

Institute of Biochemistry, University of Greifswald, Felix-Hausdorff-Str. 4, 17487 Greifswald, Germany

E-mail: keyvanmalaie@gmail.com

## Abstract

Bulk electrochemical phase transitions (EPTs) are the cornerstone of most modern electrochemical technologies, underlying many energy storage and electrocatalytic systems. Nonetheless, the fundamental mechanisms governing EPTs remain only partially understood because they involve complex interactions between phase transitions and electrochemical reactions. In this perspective, we first introduce the thermodynamics of EPTs based on the general framework of phase transitions and mixtures, followed by a discussion of their electrochemical kinetics. Finally, using recent insights from the  $\text{Ni(OH)}_2$  and  $\text{LiFePO}_4$  electrode materials, we highlight reaction hysteresis and asymmetry that challenge conventional electrochemical models. This perspective aims to inspire new fundamental research into EPTs and a fresh outlook on solid-state electrochemical reactions.

## Introduction

EPTs underpin numerous technologies such as electrodeposition, batteries, pseudocapacitors, electrochromic devices, and electrolyzers, as well as important phenomena such as corrosion<sup>[1–4]</sup>. They can be limited to one or a few monolayers of atoms on the electrode surface, such as underpotential deposition of hydrogen/metals or surface restructuring<sup>[5–7]</sup> or occur within the electrode bulk such as electrochemical ion (de)insertion, electrodeposition, and conversion reactions<sup>[8,9]</sup>.

EPTs share some features of well-established phase transitions and mixtures, e.g., water vaporization or water-oil mixtures. This similarity arises because EPTs can be viewed as mixing ions with crystal sites on the electrode or mixing oxidant (O) and reductant (R) species inside a solid. However, EPTs differ from phase mixtures and transitions in certain aspects, because

they are “reactive mixtures”, i.e., phase transition and reaction at the same time, which is coupled with electron and ion transfer across the electrode interface <sup>[10,11]</sup>.

It is commonly believed that the mechanism of electrochemical phase transition follows the nucleation and growth model <sup>[12,13]</sup>. Hence, in analogy to vaporization which is accompanied by latent heat, the formation of a new phase requires nucleation work according to the classical and atomic theory of phase formation<sup>[14]</sup>. The nucleation work is required to create new surfaces until the surface and the bulk forces balance each other. A full discussion of the mechanism of electrochemical phase formation can be found in the references <sup>[12,15–17]</sup>.

A commonly accepted view about the kinetics of EPTs is that at the beginning of the reaction, there are plenty of lattice sites for adsorption/insertion. Thus, the rate of EPT should be high at the initial stages. In the later stages, the reaction rate slows down due to the depletion of the available lattice sites. A simple model based on this statistical view is the Kolmogorov–Johnson–Mehl–Avrami (KJMA) theorem. It makes several simplifications and assumes homogeneous stochastic nucleation over a surface and a constant (or predefined) growth rate <sup>[18]</sup>. Accordingly, the fraction of the transformed phase ( $f$ ) versus time ( $t$ ) can be expressed phenomenologically as  $f=1-\exp(-kt^n)$ . However, its two parameters,  $k$  and  $n$ , are not easy to interpret in modeling EPTs.  $n$  determines the shape of the transition or growth mechanism and  $k$  is interpreted as a constant related to the rate of phase transition.

Scharifker and Motsaney (S-M) have used the Avrami equation with  $n = 1$  to model the potentiostatic current transients of electrodeposition under diffusion limitation. According to the S-M model, if the initial number of active crystal sites is large or small, the nucleation is instantaneous or progressive, respectively <sup>[12]</sup>. In the later stages, the current becomes limited by diffusion resulting in a peak in the galvanostatic current transient. The S-M model has been used successfully for the electrodeposition of mercury ions on platinum and is used widely in electrodeposition and electroplating studies <sup>[12]</sup>. However, the model parameters,  $k$ , and the initial number of active sites can depend on overpotential and other factors, leading to difficulties in their physical interpretation and deviation from experiments in electroplating studies <sup>[17,19,20]</sup>. In addition, whether EPT processes proceed via complete stochastic nucleation on surfaces according to Avrami and S-M models is open to question. Non-stochastic nucleation could be for instance due to imperfect surfaces, the presence of initial nuclei, or lattice mismatch. If nucleation phenomena were completely random, they should always start at different locations in repeating electrochemical cycles, which needs to be verified.

Herein, we obtain the electrochemical signals of EPTs from the free energies of general phase transition i.e., vaporization, to describe the different mechanisms of EPTs. Finally, we describe the unconventional electrochemical kinetics of EPTs in light of recent electrochemical models for  $\text{Ni(OH)}_2$  and  $\text{LiFePO}_4$ .

## Results and Discussion

### Phase Transition

Phase transitions can be generally described based on the free energy ( $G_m$ ) per mole at different temperatures ( $T$ ) and pressures ( $P$ ) defined as  $dG_m = -S_m dT + V_m dP$ , where  $S_m$  and  $V_m$  are the molar entropy and volume of the phase. Fig. 1a displays the free energies of two different phases, for instance, a liquid and its vapor, at different  $T$  at constant  $P$ . The curve with the steeper slope represents the vapor phase due to its larger entropy. Fig. 1b displays the entropy change associated with the transition from liquid to the vapor phase. This type of transition that is accompanied by a discontinuity in entropy is a called first-order transition, which originates from the latent heat. Alternatively, if the free energy curves in Fig. 1a are rather similar, the entropy change of the phase transition would be continuous as displayed in Fig. 1c, and it is called a second-order transition. An example of a second-order transition is the transition from ferromagnetic to paramagnetic behavior.

Fig. 1d exhibits the equilibrium  $T$ - $P$  curve, also called the coexistence curve, for the liquid-vapor system. The behavior of phase transition near the critical point can be described by Landau's theory. After the critical point, the system is homogeneous and its free energy as a function of  $x$  (an order parameter such as volume or density) is plotted in Fig. 1e. For a point on the coexistence curve, the system is heterogeneous, i.e., consists of two phases, and its free energy diagram is shown in Fig. 1f.  $x_{\text{trans}}$  signifies the volumes at which the transition between a one-phase to a two-phase system takes place.

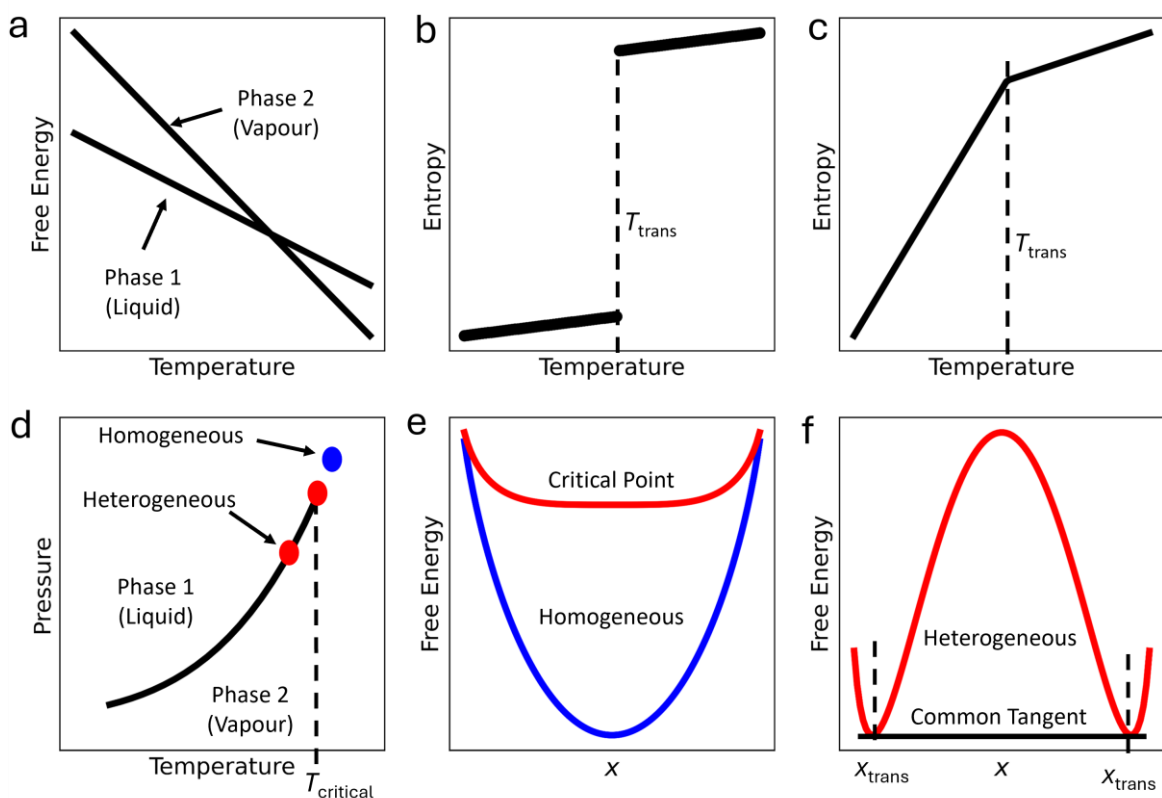


**Fig. 1** **a)** Free energy change of two phases at constant pressure, **b)** A first-order transition **c)** A second-order transition **d)** Equilibrium phase diagram of a typical liquid/vapor system based on the Clausius-Clapeyron equation, and **e)** and **f)** show the free energy profiles corresponding to the points in Fig. 1d.

These free energy plots (Fig. 1 e and f) also apply to inert phase mixtures such as the water-oil mixture, where  $x$  denotes the composition or mole fraction. For this two-component system, the free energy plots can be obtained via mixing entropy and enthalpy<sup>[21]</sup>. The region between the two minima in Fig. 1f is also known as the miscibility gap. If a homogeneous phase initially exists in this region it separates into two phases to minimize its free energy. This double-minima energy pathway is usually not accessible in electrochemical systems because they can easily become unstable under current/voltage fluctuations, causing them to go through the common tangent. Thus, this thermodynamic instability makes the free energy curves below the critical point similar to the one at the critical point.

## Thermodynamics of Electrochemical Phase Transition

EPTs are a category of phase transition where the phase transition is coupled with ion and electron transfer at the electrode interfaces. The coupling means that transferring one mole of electron and one mole of ion across the interface(s) is energetically the same process as converting one mole of a redox phase into the other. Therefore, in principle, the free energy

diagrams (Fig. 1e and f) can be used to derive and describe the electrochemical signals of EPTs, as well. This is possible by assuming  $\frac{\partial G_m}{\partial x} = \mu = -nFE$  where the symbols denote chemical potential, electron number, Faraday constant, and equilibrium potential, respectively. In this process, a formal potential corresponding to  $x = 0.5$  should be defined that depends on the pH according to the Nernst equation. Fig. 2a, the blue and red curves, exhibit diagrams of equilibrium potential versus  $x$  for a homogeneous and heterogeneous EPT obtained from the corresponding free energy curves in Fig. 1e. These curves are commonly encountered in galvanostatic charge-discharge tests of battery materials without and with phase separation, respectively. Fig. 2b displays a plot of formal potential for different solution pH, also called the Pourbaix diagram, for a typical metal oxide. The Pourbaix plots can give a very good first estimate of the type of EPT that operates under certain  $E$  and pH ranges. For instance, via obtaining experimental  $E$ -pH plots for the  $\epsilon$ -MnO<sub>2</sub> under (quasi)reversible conditions, it was verified that the dominant operating EPT in alkaline and acidic solutions are electrochemical ion (de)insertion and electrodeposition/dissolution, respectively [22].

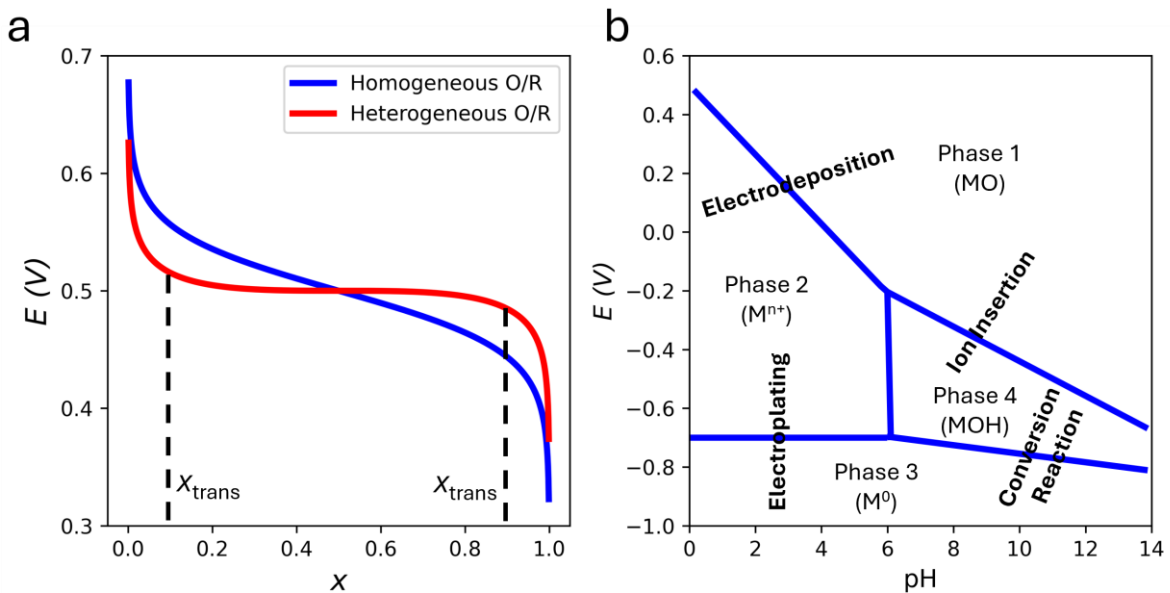


**Fig. 2 a)** Potential profiles of homogenous and heterogeneous O/R systems. **b)** A simplified phase diagram typically encountered for metal oxides and the operating EPTs. (Water oxidation and reduction are not shown)

It is possible to use the as-obtained  $E$ - $x$  plots (Fig. 2a) to derive thermodynamic cyclic voltammograms (CV) for EPTs. In Fig. 2a, the blue and red CV curves are obtained from the corresponding  $E$ - $x$  plots for EPTs under reaction control (no diffusion limitation). The narrow CV peaks correspond to a heterogeneous O/R phase transition. The broad CV curves with a full width at half maximum of about 90 mV correspond to an ideal homogenous EPT. The homogenous EPTs correspond to topological phase transitions involving a minimal change of the crystal lattice dimension during the electrochemical reaction.

If the homogenous EPT is limited by the diffusion of ions from the solution, the corresponding  $E$ - $x$  relationship constitutes the boundary condition for Fick's second law [23]. The CV curve of this EPT is exhibited in Fig. 3b. The reduction and the oxidation tails at the potential limits do not go to zero current within experimental time but rather a plateau due to the assumed semi-infinite linear diffusion.

Often, EPTs are more complicated than the three cases presented in Fig. 3a and b mainly due to phase separation during reaction. As a result, EPTs can very easily show electrochemical hysteresis similar to magnetic hysteresis. Fig. 3c exhibits the representative CV cycle of reaction-controlled EPTs with strong (red curve) and weak hysteresis (blue curve). The oxidation and reduction potentials appear at different locations in this reaction-controlled EPT. This hysteresis is accounted for in the free energy diagrams by including an asymmetric energy term for the surface energy between the O and R phases. Accordingly, the surface energy for oxidation and reduction are different because oxidation and reduction go through different reaction pathways (reaction asymmetry), resulting in different energy landscapes [21]. In other words, when EPTs occur close to or below the critical point (Fig. 1d), the relative contribution of solid solution and phase separation pathways depends on the direction of the reaction. A reason for this complication is that the EPT cannot pass through the common tangent to the other side and phase boundaries remain at the end of oxidation/reduction time. It is noted here, that this hysteresis effect is not shared by the phase diagrams displayed in Fig. 1, because water always vaporizes and condenses at 100 °C at 1 atm, regardless of direction.

A comparison of these hysteretic CV curves (Fig. 3c) with the experimental CV curves of the CoOOH/CoO<sub>2</sub> and Ni(OH)<sub>2</sub>/NiOOH indicates that the phase separation and hysteresis can originate from the different ionic radii of the metallic centers of the O and R species<sup>[21]</sup>. A similar observation can also be made for the widely studied phase separation in the LiFePO<sub>4</sub>

cathode [24], in which the ionic radius of Fe can change about  $0.14 \text{ \AA}$  [25] during charge and discharge.

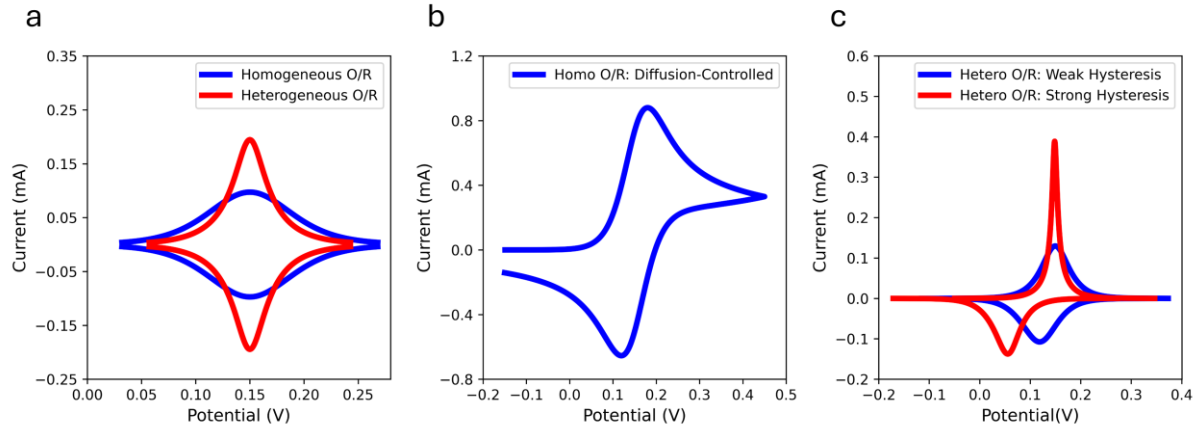


**Fig. 3** Thermodynamic CVs of EPT **a)** reaction-controlled EPTs, **b)** diffusion-controlled homogenous EPT, and **c)** reaction-controlled homogeneous and heterogeneous EPTs with different levels of electrochemical hysteresis

## Kinetics of Electrochemical Phase Transition

We have recently introduced a nonthermodynamic model based on autocatalytic growth to describe the kinetics and mechanism of EPTs [26]. In this model, the rate of the reaction is not determined by stochastic nucleation and diffusion-limited growth, as suggested by the S-M model, but it is determined by the interactions between O and R species. The reaction rate depends on the different stages ( $x$ ) of particle growth, making it a size-dependent growth rate equal to  $kx(1-x)^m$  as displayed in Fig. 4. If the interaction between O and R crystal units are 1 to 1, i.e.,  $m=1$ , the EPT is homogeneous as represented with the grey curve. In addition, for homogeneous EPTs, the interaction parameter,  $k$ , is identical for both oxidation and reduction directions. When  $m>1$ , the EPT is heterogeneous and involves phase separation (red curve). An inherent outcome of phase separation in this model is that the EPT is autocatalytic in the direction of phase formation (ion deinsertion) and autoinhibitory in the direction of phase dissolution (ion insertion).

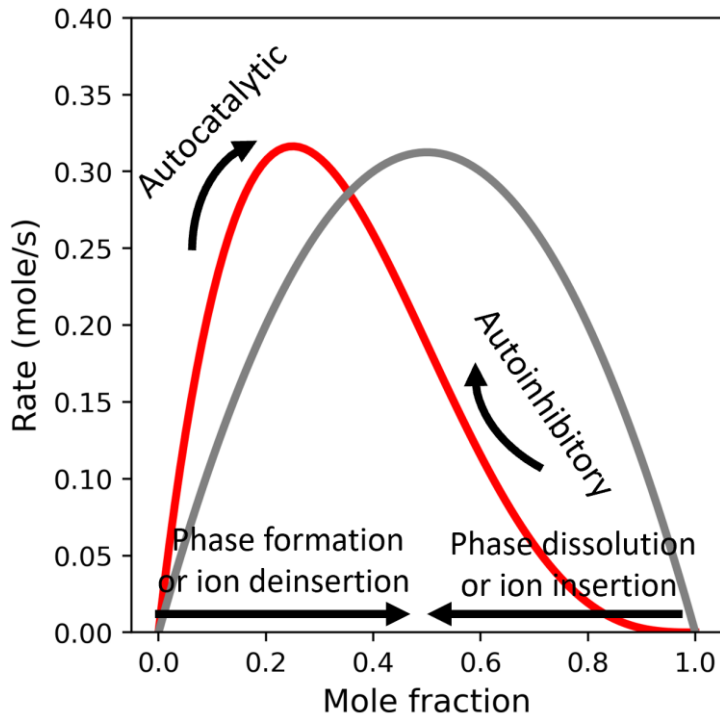


**Fig. 4.** Rate profiles of a homogenous (grey) and heterogeneous (red) EPT based on a reaction-controlled model according to the rate equation  $kx(1-x)^m$  with  $m = 1$  and  $3$ , respectively, and  $k_{\text{insert}} = k_{\text{deinsert}}$  for both systems.

This simple model is used to explain the (de)protonation mechanism of  $\text{Ni(OH)}_2$  thin films during CV [26]. Fig. 5a exhibits the first two CV cycles of  $\text{Ni(OH)}_2$  in 0.1 KOH at a scan rate of 2 mV/s and its comparison with the heterogeneous model. The sharp rise of the oxidation peak (an asymmetric peak) and its higher current compared to the reduction peak is due to the strong autocatalytic deprotonation of  $\text{Ni(OH)}_2$  to  $\text{NiOOH}/\text{NiO}_2$ . The fact that the second oxidation peak appears at lower potentials is due to the residual  $\text{NiOOH}/\text{NiO}_2$  remaining from the first cycle. Thus, the formation of  $\text{NiOOH}/\text{NiO}_2$  particles promotes the deprotonation rate as expected for an autocatalytic reaction. This effect of the initial amount of the product on the reaction rate is similar to the effect of nucleation overpotential on reaction rate in the electrodeposition (electroplating) of metals [27].

Fig. 5b (red curves) shows the second CV cycles of the same  $\text{Ni(OH)}_2$  at two different scan rates at 2 and 5 mV/s. Interestingly, the effect of scan rate for the deprotonation and protonation peaks are different. At a scan rate of 2 mV/s, the autocatalytic model (blue curves) simulates the CV curve with  $k_{\text{deinsert}}/k_{\text{insert}} = 2.5$ , but at a scan rate of 5 mV/s this parameter needs to be reduced to 1.4 to simulate the CV curve. The lower value of this parameter indicates less

phase separation during deprotonation at higher scan rates, and hence, lower reaction asymmetry. Bazant et al. [28] have for the first time reported this effect of charge-discharge rate on the reaction pathway via the galvanostatic curves of the LiFePO<sub>4</sub> (de)lithiation [29].

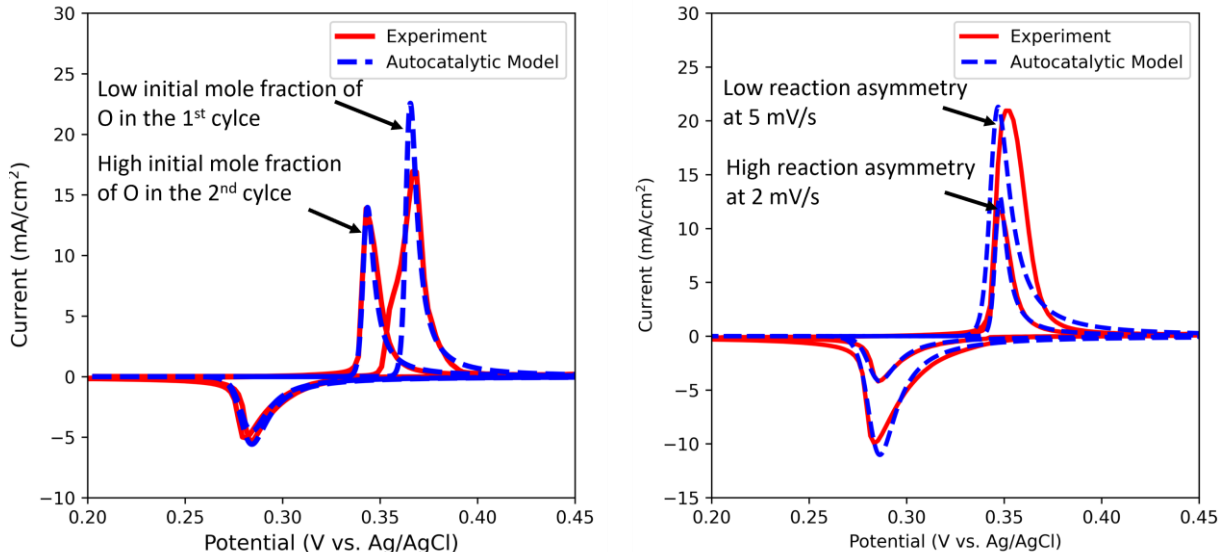


**Fig. 5** Comparison of experimental CV of Ni(OH)<sub>2</sub> thin film in 0.1 KOH with autocatalytic deprotonation and autoinhibitory protonation model. Comparison of model with **a)** the first and second cycles with an initial mole fraction of O equal to  $5 \times 10^{-8}$  and  $2.6 \times 10^{-3}$ , respectively, and **b)** two cycles at 2 and 5 mV/s with  $k_{\text{deinsert}}/k_{\text{insert}}=2.5$  (high reaction asymmetry) and  $k_{\text{deinsert}}/k_{\text{insert}}=1.4$  (low reaction asymmetry), respectively. Reproduced from ref. [26] with permission from the Royal Society of Chemistry.

Fig. 6 shows *In situ* X-ray microscopy images of LiFePO<sub>4</sub> at two different galvanostatic charge/discharge rates [29]. When the charge/discharge rate is low (0.15 C), the delithiation exhibits a clear phase separation as an intercalation wave, but the lithiation is more homogeneous across the particle surface area. Within this regime of charge-discharge rates, the process is reaction-controlled featuring autocatalytic delithiation and autoinhibitory lithiation. However, when the charge-discharge rate is increased to 1.5C and 4C, the delithiation becomes more homogenous across the particle, hence reducing the reaction asymmetry. Thus, the phase transition behavior of LiFePO<sub>4</sub> is in agreement with that of Ni(OH)<sub>2</sub> presented in Fig. 5.

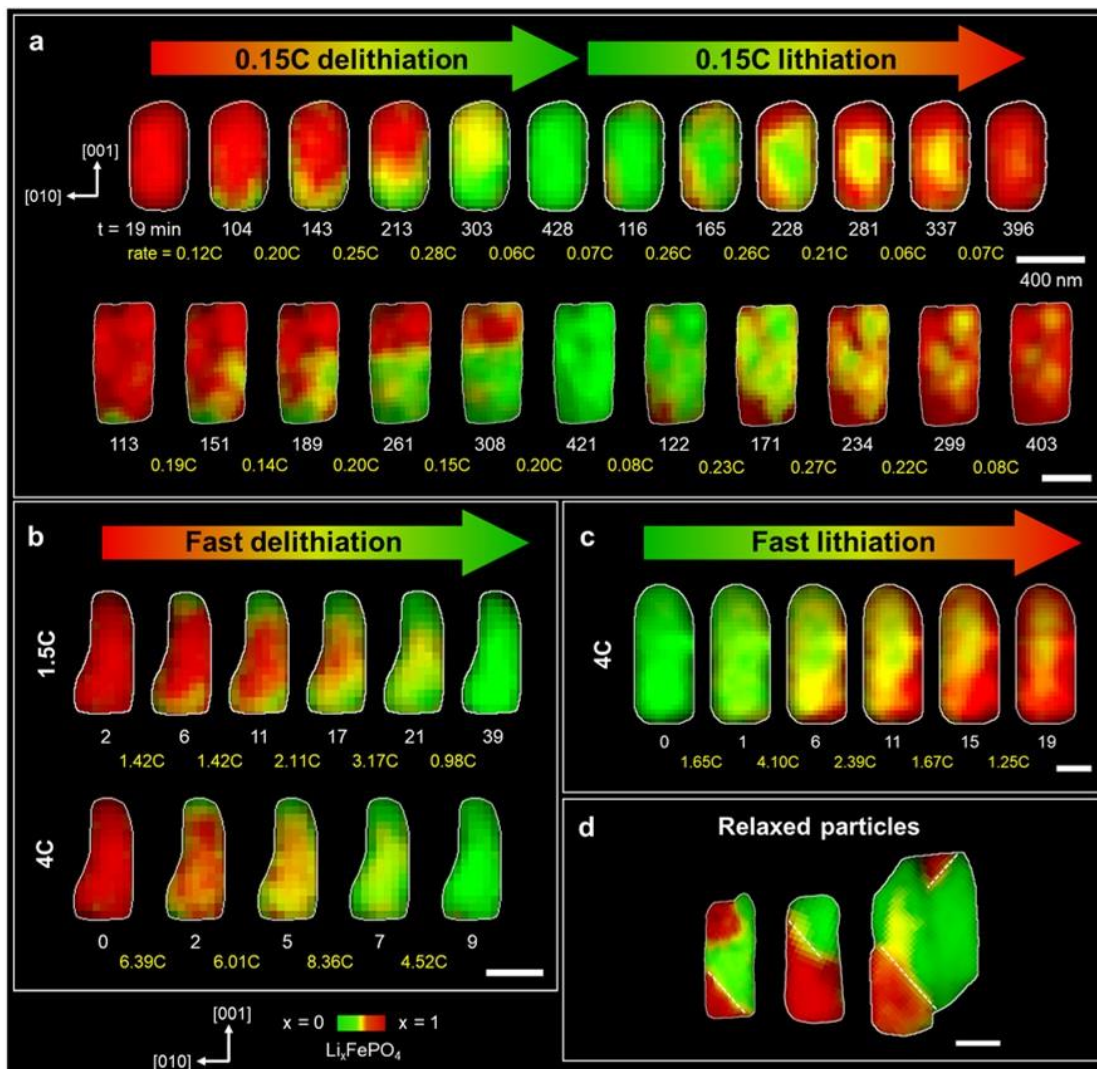


**Fig. 6** Operando X-ray scanning transmission microscopy of LiFePO<sub>4</sub> primary particles. Li composition maps of particles during (de)lithiation at rates of **(a)** 0.15C and **(b and c)** 1.5C, 4C. Red and green colors indicate Li-rich and Li-poor phases, respectively. White and yellow numbers are indicators of time **(d)** Ex situ Li composition maps of relaxed particles. Scale bars is 400 nm. Reproduced from ref. <sup>[29]</sup> with permission from the Royal Society of Chemistry

## Conclusion and Future Prospects

Phase diagrams are basic tools for studying phase transitions and mixtures and have been widely applied to electrochemical phase transitions (EPTs). While straightforward to use, they fall short of capturing the complexities inherent in EPTs, particularly because they do not incorporate reaction dynamics or charge transfer in their conventional form. As a result, they offer limited insights into key features of EPTs such as kinetics, hysteresis, reaction asymmetry, and memory effects. Emerging research further highlights the influence of particle size<sup>[30]</sup>,

crystal structure, charge-discharge rates, overpotential, and potential scan rate on reaction pathways—factors that phase diagrams do not address. Moreover, the effects of pH and electrolyte ions on EPT mechanisms remain largely unexplored. Implementing EPT models in non-aqueous batteries also requires accounting for the solid–electrode interphase (SEI), which significantly alters reaction mechanisms and kinetics. Consequently, there is currently no general framework to predict the electrochemical signals of EPTs based on structural parameters and experimental conditions.

Nucleation–growth models have provided valuable insights into the early stages of electrocrystallization, yet they face two main limitations in EPT studies. First, they are typically limited to initial phase formation and do not describe the growth of larger particles. Second, they generally treat only one direction of the transition—often the formation phase—while in real electrochemical systems both directions, oxidation and reduction, are equally important. These constraints hinder their ability to explain anomalous behaviors observed in EPTs. Nonetheless, nucleation-growth models remain useful in EPT studies, as they are founded on fundamental thermodynamic principles.

In the absence of a comprehensive growth theory for EPTs, empirical models like the Avrami equation are sometimes used. However, their application is restricted by the lack of clear physical meaning behind their parameters and the stochastic presumption, limiting the mechanistic insights that they can provide.

Finally, the current perspective attempted to reveal the more hidden sides of the EPTs such as reaction hysteresis and asymmetry using phase diagrams, electrochemical modeling, and platform EPT materials such as  $\text{Ni(OH)}_2$  and  $\text{LiFePO}_4$ . We hope that it can motivate more fundamental research into EPTs. Extensive experimental data is needed to clarify the validity and scope of present models, and more advanced theories of EPT are needed to explain the dependence of EPTs on material structure and experimental parameters. An improved understanding of EPTs will pave the way for advancing current electrochemical energy technologies.

## Conflicts of Interests

There are no conflicts to declare.

## Acknowledgment

The author acknowledges the Alexander von Humboldt Foundation and the University of Greifswald. He appreciates Prof. Uwe Schöder for his insightful discussions and motivation to write this paper.

## References

- [1] V. V. Kharton, *Solid State Electrochem. I Fundam. Mater. their Appl.* **2009**, 1–506.
- [2] G. Wittstock, in *Lehrb. Der Elektrochimie*, Wiley-VCH, Weinheim, **2023**, p. 536.
- [3] P. J. Gellings, *The CRC Handbook of SOLID STATE Electrochemistry*, CRC Press, Boca Raton FL, **1997**.
- [4] A. J. Bard, L. R. Faulkner, H. S. White, *Electrochemical Methods : Fundamentals and Applications, Third Edition*, Wiley, Hoboken, NJ SE -, **2022**.
- [5] A. A. Kornyshev, I. Vilfan, *Electrochim. Acta* **1995**, 40, 109–127.
- [6] D. Cheng, Z. Wei, Z. Zhang, P. Broekmann, A. N. Alexandrova, P. Sautet, *Angew. Chemie* **2023**, 135, 1–7.
- [7] Z. Zhang, Z. Wei, P. Sautet, A. N. Alexandrova, *J. Am. Chem. Soc.* **2022**, 144, 19284–19293.
- [8] F. Scholz, *Electroanalytical Methods: Guide to Experiments and Applications, Second Edition*, Springer, Heidelberg, **2010**.
- [9] A. Doménech-Carbó, *J. Phys. Chem. C* **2022**, 126, 11822–11832.
- [10] M. Z. Bazant, *Faraday Discuss.* **2017**, 199, 423–463.
- [11] H. Zhao, M. Z. Bazant, *Phys. Rev. E* **2019**, 100, 1–11.
- [12] J. Mostany, B. Scharifker, *Encycl. Electrochem.* **2010**, 512–540.
- [13] M. S. Whittingham, *Chem. Rev.* **2014**, 114, 11683–11720.
- [14] V. Tsakova, *J. Solid State Electrochem.* **2020**, 24, 2183–2185.
- [15] A. Milchev, *Electrococrystallization: Fundamentals of Nucleation and Growth*, Kluwer Academic Publishers, Boston, Mass., **2002**.
- [16] A. Milchev, *Nanoscale* **2016**, 8, 13867–13872.
- [17] A. Nakova, B. Rangelov, V. Tsakova, *J. Electrochem. Soc.* **2025**, 172, 12510.
- [18] M. Fanfoni, M. Tomellini, *NUOVO Cim.* **1998**, 20, 1171–1182.
- [19] M. Pise, M. Muduli, A. Chatterjee, B. P. Kashyap, R. N. Singh, S. S. V. Tatiparti, *Results in Surfaces and Interfaces* **2022**, 6, 100044.

- [20] E. R. Cooper, M. Li, I. Gentle, Q. Xia, R. Knibbe, *Angew. Chemie* **2023**, *135*, DOI 10.1002/ange.202309247.
- [21] K. Malaie, F. Scholz, U. Schröder, *ChemElectroChem* **2023**, *10*, e202201118.
- [22] K. Malaie, F. Scholz, U. Schröder, H. Wulff, H. Kahlert, *ChemPhysChem* **2022**, *23*, e202200364.
- [23] K. Malaie, **n.d.**, DOI <https://doi.org/10.48550/arXiv.2503.14758>.
- [24] J. Lim, Y. Li, D. H. Alsem, H. So, S. C. Lee, P. Bai, D. A. Cogswell, X. Liu, N. Jin, Y. Yu, N. J. Salmon, D. A. Shapiro, M. Z. Bazant, T. Tyliszczak, W. C. Chueh, *Science (80-. ).* **2016**, *353*, 566–571.
- [25] R. D. SHANNON, *Acta Cryst.* **1976**, *A32*, 751–767.
- [26] K. Malaie, *Phys. Chem. Chem. Phys.* **2023**, *25*, 30606–30611.
- [27] A. A. Isse, S. Gottardello, C. Maccato, A. Gennaro, *Electrochem. commun.* **2006**, *8*, 1707–1712.
- [28] P. Bai, D. A. Cogswell, M. Z. Bazant, *Nano Lett.* **2011**, *11*, 4890–4896.
- [29] B. Koo, J. Chung, J. Kim, D. Fragedakis, S. Seo, C. Nam, D. Lee, J. Han, S. Jo, H. Zhao, N. Nadkarni, J. Wang, N. Kim, M. Weigand, M. Z. Bazant, J. Lim, *Energy Environ. Sci.* **2023**, *4*, DOI 10.1039/D3EE00341H.
- [30] P. C. Chen, M. Gao, C. A. McCandler, C. Song, J. Jin, Y. Yang, A. L. Maulana, K. A. Persson, P. Yang, *Nat. Nanotechnol.* **2024**, DOI 10.1038/s41565-024-01626-0.